Ocean Engineering 145 (2017) 237–249

Contents lists available at ScienceDirect

Ocean Engineering

journal homepage: www.elsevier.com/locate/oceaneng

Simplified analysis of the influence of strain localization and asymmetric damage distribution on static damaged polyester rope behavior

Juan Felipe Beltrán [a,*], Nicolás Ramírez [b], Eric Williamson [c]

[a] Dept. of Civil Engineering, University of Chile, Blanco Encalada # 2002 of. 440, Santiago, Chile
[b] Dept. of Civil Engineering, University of Chile, Blanco Encalada # 2002, Santiago, Chile
[c] Dept. of Civil Engineering, University of Texas at Austin, 1 University Station C1748, Austin, TX, 78712-0273, USA

ARTICLE INFO

Keywords:
Damage
Synthetic-fiber rope
Numerical simulation
Rope failure
Rope response

ABSTRACT

In this paper, two factors that govern the response of damaged ropes are numerically examined independently: strain localization and asymmetric damage distribution. These two mechanisms are studied by using two nonlinear mechanical models that account for the strain localization around the failure site due to frictional effects (*SLM*) and the presence of unbalanced radial contact forces within a rope cross-section due to the asymmetry in damage distribution (*ADDM*). These models are applied to an available set of static tension tests on asymmetrically damaged, large-scale polyester ropes. The initial damage level of the rope cross-sections and rope diameters varied from 5% to 15% and from 32 mm to 166 mm, respectively. A semi-analytical proof is given to show that *SLM* and *ADDM* provide upper and lower bounds, respectively, to the damaged response of the ropes analyzed. Results indicate that, relative to the intact rope, the *SLM* predicted a reduction in rope capacity similar to the damage level and a maximum reduction in rope deformation capacity equal to 16% for an effective damage level equal to 25%. Conversely, the *ADDM* predicted a reduction in rope residual strength slightly greater than the damage level and a maximum reduction in deformation capacity equal to 3%.

1. Introduction

A rope is a slender and flexible structural element used in many engineering applications including cranes, bridges, electrical conductors, mine hoisting, offshore mooring, and so on. Ropes manufacturers provide different configurations of ropes suited for the wide aforementioned range of usage, having a different number and arrangement of rope components, which can be made of different materials such as metal, natural, and synthetic fibers, within the rope cross-section (Foster, 2002; McKenna et al., 2004).

During rope operational service, mechanical demands, abrasion and environmental interaction (corrosion, chemical, ultra-violet light, heat exposure, etc.) continuously degrade the mechanical properties of individual rope components. This degradation process could result in the rupture of some rope components, which could eventually lead to rope failure. Damage to ropes, which could start during rope transportation and installation, is complex and different for each rope application, revealing the local operating parameters and the characteristics of the rope selected (Chaplin, 2005).

Experimental (Hankus, 1981; Cholewa and Hansel, 1981; Chaplin and Tantrum, 1985; Cholewa, 1989; Evans et al., 2001; Li et al., 2002; and Ward et al., 2006; Liu et al., 2015; Lian et al., 2015 among others) and theoretical (Lanteigne, 1985; MacDougall and Bartlett, 2005, 2006; Beltran and Williamson, 2010, 2011; Beltran and Vargas, 2012; and Beltran and De Vico, 2015 among others) studies, mainly conducted on steel wire ropes and synthetic fiber ropes, have intended to determinate the ability of particular types of rope constructions to withstand damage (i.e., damage-tolerance property). The results of previous studies have shown that the impact of broken rope components on overall rope response (stiffness, residual strength, deformation capacity, and deformed configuration) depends on the length of the rope, number of broken rope components (degree of damage or damage level), type of rope construction, and their distributions throughout the rope cross-section (symmetric and asymmetric) and along the rope length.

In the context of analyzing damaged rope behavior, the damage-tolerance property is an essential parameter for rope design, rope evaluation during operational service, and for developing discard criteria according to rope usage based on the residual strength and deformation capacity a degraded (damaged) rope can sustain. Thus, the effects of the multiple degrading factors on rope response and the complex interactions

* Corresponding author.
E-mail addresses: jbeltran@ing.uchile.cl (J.F. Beltrán), ramirez.guzman.n@gmail.com (N. Ramírez), ewilliamson@mail.utexas.edu (E. Williamson).

http://dx.doi.org/10.1016/j.oceaneng.2017.09.006
Received 2 September 2016; Received in revised form 5 September 2017; Accepted 6 September 2017
Available online 18 September 2017

between them should be understood in order to establish the appropriate rope inspection methods and discard criteria, and in this way, extend rope service life (Chaplin, 2005).

In this paper, two mechanisms that rule the behavior and failure of damaged ropes are numerically examined individually: strain localization and asymmetric damage distribution. The former mechanism is accounted for by using the numerical model proposed by Beltran and Williamson (2011) in which the rope analysis is linearized by discretizing the rope into a series of two-noded axial-torsional elements whose formulation accounts for material and geometric nonlinearities. The discretization of the damaged rope depends upon the potential incremental contribution of broken rope components to overall rope response due to frictional forces that defines the length over which damage propagates along the length of a rope (the so-called damage length). To account for the latter mechanism, the model proposed by Beltran and De Vico (2015) is extended to account for multi-level rope geometry (more than one helical structure can be found in rope construction). The damaged rope is assumed to behave as a nonlinear beam under biaxial bending and axial load with Bernoulli's kinematic hypothesis. A semi-analytical proof is given to show that strain concentration and asymmetric damage distribution capacity curves provide upper and lower bounds, respectively, to damaged rope response. Based on this proof, conclusions can be drawn regarding which mechanism has more influence on the behavior of a particular damaged rope in terms of its stiffness, residual strength, and deformation capacity. Comparisons with available static tension tests on large-scale ropes (diameters vary from 32 mm to 166 mm) asymmetrically damaged (initial damage level varies from 5% to 15%) polyester ropes (Ward et al., 2006) are performed to validate the proposed models and to explain the measured damaged ropes responses.

2. Damaged rope response simulation

2.1. Strain localization model (SLM)

Beltran and Williamson (2011) presented a numerical model to estimate the effect of broken rope components on overall rope response. This proposed model relies on the ability of broken rope components to carry their proportionate share of axial loads over a distance measured from the failure region, which is referred as the *recovery length* (*rl*) (Raoof, 1991). The ability of a failed rope component to resume carrying load is due to frictional forces, which depend on the presence of contact forces between rope components (due to their helical nature and/or rope jacket confinement) and the surface characteristics (i.e., coefficient of friction) of the components in contact. The model assumes axisymmetric response, accounts for the type of rope construction, damage level, and damage distribution along the length of the rope. A limitation of this model, however, is that it ignores any loss of symmetry due to the failure of any rope components. If the recovery length value is admissible (i.e., within the physical length constraints of the rope being analyzed), a damaged rope is discretized along its length into two-noded axial-torsional elements, which provides a means for representing a weakened cross-section acting over a localized region. For the purpose of this study and in order to simplify the analysis, the gradual increase in load carried by broken rope components is ignored. Thus, only the full value of axial load at distances outside admissible recovery length values are taken into consideration. The proposed model accounts for the geometric nonlinearity of a rope's displacement and the potential nonlinearity of the constitutive response of the components that form a rope. In addition, the potential confinement effect of a rope jacket on rope components is included in the proposed model by assuming the rope jacket behaves like a thin-walled tube.

The formulation of the *SLM* is briefly described for completeness, but full details of its formulation can be found in the corresponding references. In Fig. 1a, the two-noded axial-torsional element used to discretize damaged rope length is presented. Each element includes two degrees of freedom at each node: axial displacement (u_i) and axial rotation (ϕ_i). Associated with these degrees of freedom are the corresponding axial force N_i and torsional moment T_i. For the sake of the model description, consider that the failure region is located near the rope midspan and broken rope components (identified in black color) fully develop their recovery length values. In this case, damaged rope is a non-prismatic rope discretized into three two-noded axial-torsional elements in which the length L_{S2} represents the damage length (broken components do not contribute to rope response), and its value is equal to $2rl$. In elements of lengths L_{S1} and L_{S3}, which are equal due to the symmetry of the model, broken components fully contribute to rope response because they have entirely developed their *rl* values as depicted in Fig. 1b (they are not in black color).

As explained by Beltran and Williamson (2011), the tangent stiffness matrix of each axial-torsional element S_i is computed, and then each tangent stiffness matrix is assembled to obtain the tangent stiffness matrix of the entire rope. For each axial-torsional element, equilibrium considerations are used to describe, in terms of only two independent degrees of freedom (referred to as the "essential set"- axial deformation ($u_3 - u_1$) and the axial rotational deformation ($\phi_4 - \phi_2$)), its response. Consequently, a 2 × 2 stiffness matrix is computed having the following form:

$$[\boldsymbol{k_{sr}}]_i = \begin{bmatrix} k_{\lambda\lambda} & k_{\lambda\eta} \\ k_{\eta\lambda} & k_{\eta\eta} \end{bmatrix}_i \tag{1}$$

where the subscripts λ and η are associated with the axial strain and the rate of twist, respectively, of the cross-section of element S_i. No closed-form expressions exist to compute the stiffness coefficients due to the nonlinear geometry and (eventually) nonlinear constitutive response of the rope components. Accordingly, a numerical procedure is implemented, based upon the centered differentiation formula, to compute these terms. The 4 × 4 tangent stiffness matrix $[\boldsymbol{K_{sr}}]_i$ of each axial-torsional element S_i, associated with the degrees of freedom u_1, ϕ_2, u_3 andϕ_4 (referred as to the "complete set") described in Fig. 1a, can be obtained through equilibrium consideration of each element for assembling the tangent stiffness matrix of the entire rope. A summary of the

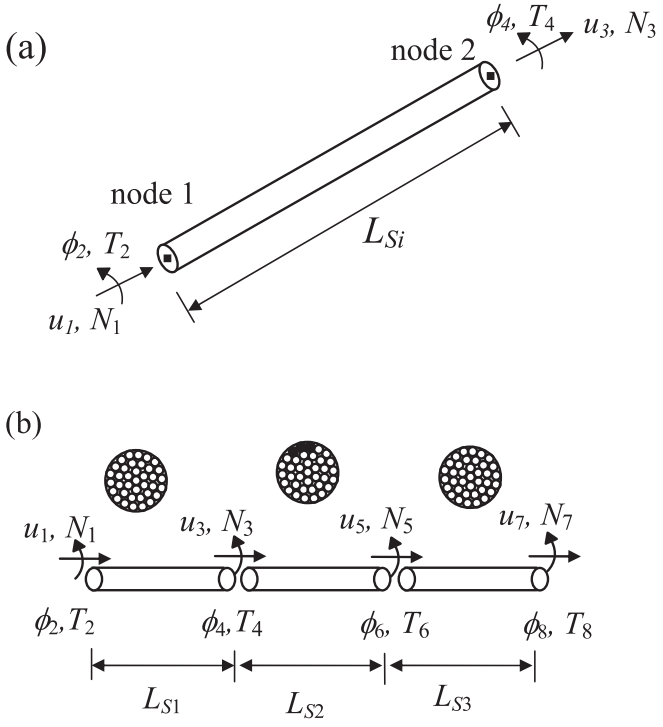

Fig. 1. (a)Two-noded axial-torsional element; (b) damaged rope discretization.

numerical scheme implemented to compute the stiffness matrices $[\boldsymbol{k}_{sr}]_i$ and $[\boldsymbol{K}_{sr}]_i$, for each axial-torsional element S_i and the values of the increments in axial displacements and axial rotations as well as the increments in external loads (axial forces and torsional moments), is provided in Appendix A.

The numerical algorithm of the *SLM* is based upon a displacement control analysis scheme in which increments in axial displacement are prescribed for the rope. The size of these increments is constrained by the computed axial strain values of the smallest defined structure (i.e., rope components for which material law is known) that comprises the rope. These values should not exceed a maximum value arbitrarily set for the algorithm (typically 2% of the failure axial strain value). If this criteria is not met or the numerical algorithm of the *SLM* does not converge (Beltran and Williamson, 2011) for a particular incremental step of the analysis, sub-steps are performed by continuously bisecting the increment in axial rope displacement until both increment size criteria and convergence of the algorithm are achieved. The maximum strain failure criteria is adopted to determine whether any rope component failure initiated and consequently, at that strain level, to estimate the residual strength and deformation capacity of the damaged rope.

According to the *SLM* formulation, the predicted response curve of a damaged rope (Fig. 1b) starts approaching to the response curve of the intact (i.e., undamaged) rope as the value of the damage length gets smaller relative to the length of the rope (damaged rope response gets stiffer), provided all broken components fully develop their recovery length values. Given an increment in the displacement of a damaged rope, the increment in the external load (axial force and torsional moment) can be obtained through the following expression:

$$\begin{Bmatrix} \Delta F \\ \Delta T \end{Bmatrix}_J = \left([\boldsymbol{k}_{sr}]_{\text{int}}\right)_{J-1} \begin{Bmatrix} \Delta u \\ \Delta \varphi \end{Bmatrix}_J \tag{2}$$

where ΔF_J and ΔT_J are the increments in axial force and torsional moment, respectively, and Δu_J and $\Delta \phi_J$ are the specified axial

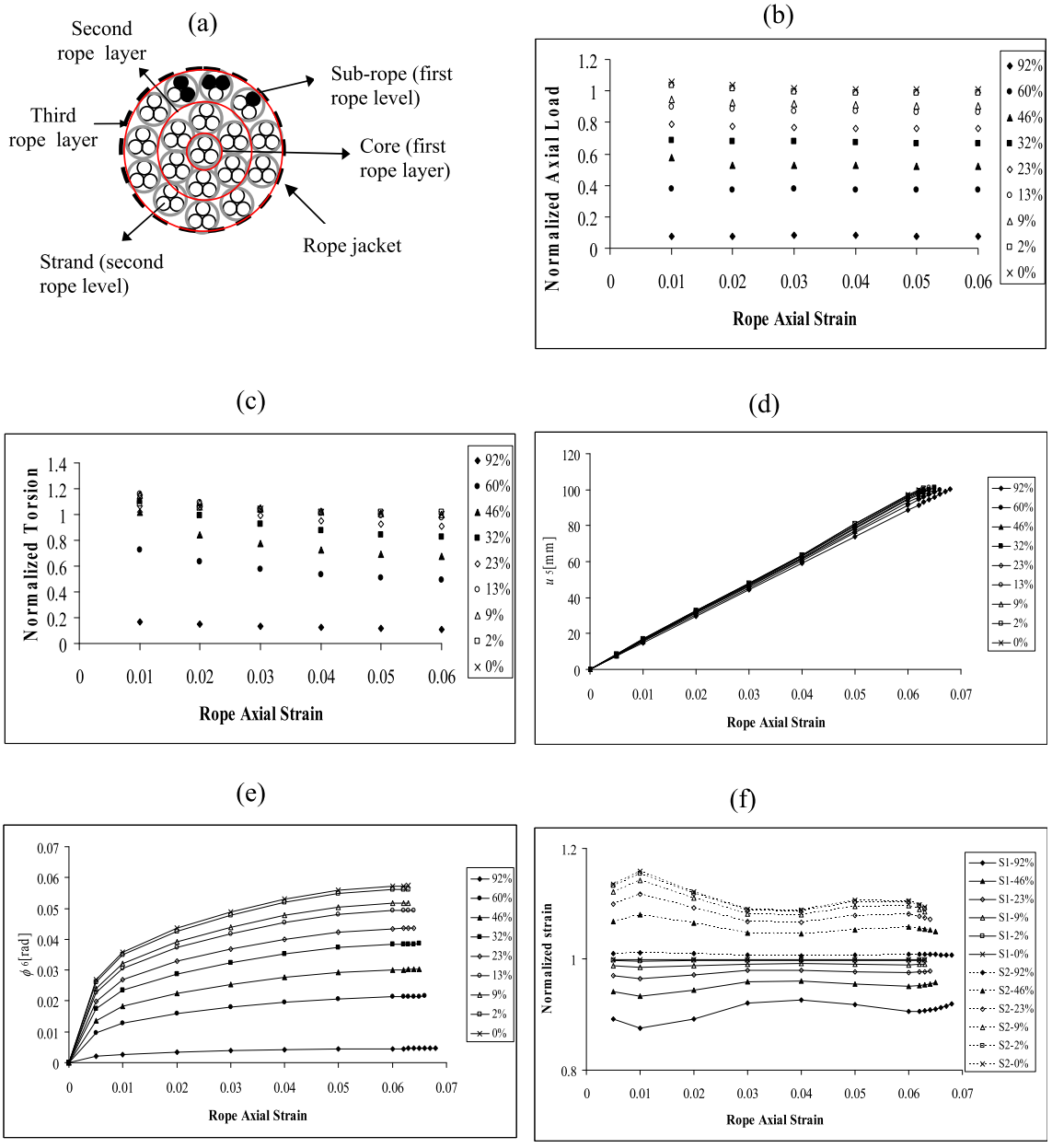

Fig. 2. (a) Damaged rope cross-section; (b) axial load convergence; (c) torsional moment convergence; (d) and (e) dependence of the axial displacement and axial rotation of the damage length respectively; (f) convergence of the strain distribution along the rope length.

displacement and axial rotation, respectively, of the rope in the *Jth* incremental step of the analysis. The parameter $([\boldsymbol{k}_{sr}]_{\text{int}})_{J\text{-}1}$ is the tangent stiffness matrix of an intact two-noded axial-torsional element computed by considering the rope configuration of the (*J*-1)th incremental step (known configuration). It is important to point out that this approach is only valid for estimating the stiffness, axial load, and torsional moment of the damaged rope; the strain distribution along the length of the rope depends on the solution of the entire *SLM* depicted in Fig. 1a as discussed later in the paper.

Provided all broken components develop admissible recovery length values, to study the dependence of damaged rope response on damage length and to prove that the corresponding damaged capacity curve converges to the intact one as the damage length gets smaller relative to the length of the rope, a particular damaged rope analysis is presented. Consider the two-level three-layer damaged rope cross-section depicted in Fig. 2a. Rope level refers to the number of structures in the hierarchy of components that exist in the rope. This rope cross-section is formed by 18 parallel polyester sub-ropes (i.e., the sub-ropes are not twisted together in a helical fashion forming the first level of the rope), arranged in three layers (red circles in Fig. 2a), and confined by a polyester jacket (dashed black circle in Fig. 2a). Layers refer to the number of concentric circles of components wrapped around the core. In the terminology used in this study, the core is always considered to be the first layer (Fig. 2a). Each sub-rope itself, however, is built by twisting three strands (second rope level) together around a fictitious straight core. The rope has a specified undamaged breaking strength (SBS) of 35 tonnes (343.2 kN) and a diameter equal to 32 mm. Five strands of three adjacent sub-ropes have been cut (colored black) prior to loading to inflict approximately 10% of damage to the rope cross-section as reported by Ward et al. (2006). These researchers concluded that for this particular type of rope construction (parallel sub-rope configuration), a strain concentration zone around the failure section may be induced by rope jacket confinement, type of rope construction (sub-ropes formed by twisted strands), and rope terminations.

The convergence of the axial load and torsional moment provided by the *SLM* (N_7 and T_8 in Fig. 1b, respectively) is studied by varying the percentage of the damage length of the rope (length L_{S2} in Fig. 1b) relative to the total length of the rope. The magnitudes of these parameters, normalized by the corresponding quantities assuming an intact rope response (Eq. (2)), are presented in Fig. 2b and c for prescribed values of the rope axial strain (horizontal axis of the plots). For modeling purposes, boundary conditions of the model considers one end section of the rope fully clamped and the other end to have a uniformly increasing axial displacement history specified with the cross-section prevented from rotating. For this particular analysis, the percentage of the damage length of the rope ranges from 0% to 92% for both variables, considering a wide range of axial strain values (from 0 to 0.06), in which 0.07 is the failure rope axial strain value experimentally obtained by Ward et al. (2006) for the intact rope case. Both normalized parameters approach 1.0, and the difference between two consecutive values becomes smaller as the percentage of the damage length gets smaller relative to rope length for the entire range of rope axial strain values considered. This means that damaged rope response, in terms of the stiffness and external loads (axial load and torsional moment), can be estimated by the model of the intact rope given by Eq. (2) for prescribed values of the rope axial strain as the percentage of the damage length gets smaller relative to rope length. Along with the convergence of the damaged rope stiffness to intact rope stiffness, the kinematics variables u_5 and ϕ_6 (as well as u_3 and ϕ_4 due to symmetry conditions) associated with the damage length of the rope (Fig. 1b) become dependent on the rope axial strain (variables u_1 and u_7 in Fig. 1b) as presented in Fig. 2d and e. The relationships between both kinematic variables u_5 and ϕ_6 and rope axial strain converge to a single curve considering a wide range of rope axial strain values; thus, the independent degrees of freedom of the damaged rope model are u_1 and u_7 (values of ϕ_2 and ϕ_8 are set equal to zero in this numerical example), which are solely related to the intact two-noded axial-torsional element as the percentage of the damage length gets smaller relative to rope length.

In terms of the strain distribution along the length of the damaged rope, strain localization develops around the failure region as shown in Fig. 2f, in which the strain values developed in the damaged (S2) and intact (S1) elements are normalized by the prescribed axial rope strain values. Strains developed in the S2 element (dashed curves) are greater than both the prescribed rope axial strains and the strains developed in the S1 (also S3 according to Fig. 1b) element (solid curves), in which the latter are smaller than the prescribed rope axial strain values but converge to them as the percentage of the damage length gets smaller relative to rope length (ratio of the plotted values approaches 1.0). If the damaged rope is transformed into an equivalent prismatic rope based on the damaged element properties (S2), the effective length of this equivalent rope is smaller than the original one to match the (original) non-prismatic damaged rope stiffness. Thus, the axial displacement prescribed to the equivalent non-prismatic rope is distributed over a smaller length, inducing higher axial strain in the damaged element (S2) than the value prescribed for the non-prismatic damaged rope. By axial equilibrium (elements S_i are in series configuration), axial strains developed in the undamaged elements (S1 and S2 in Fig. 1b) are smaller than the ones developed in the damaged length. Additionally, as the percentage of the damage length (S2) decreases relative to the rope length, the effective length of the equivalent prismatic rope gets smaller as well. The axial strain computed for the equivalent prismatic rope gets higher (the axial displacement specified for the damaged rope is distributed over a smaller length) and consequently its failure strain is reached for smaller values of the axial displacement specified for the (original) damaged rope. As such, axial strains in the damaged element S2 also increase as the percentage of the damage length gets smaller relative to rope length, converging to an upper bound curve for a wide range of rope axial strain values and controlling the deformation capacity of the entire damaged rope. The curves shown in Fig. 2f (and also in Fig. 2d and e) are plotted up to the onset of damaged rope failure (associated with the maximum load carrying capacity and its corresponding strain) to be consistent with previous researchers (Li et al., 2002; Ward et al., 2006; Beltran and Williamson, 2011; Beltran and Vargas, 2012; among others) in which the subsequent fracture process of the rope cross-section is not part of this study. The reduction in the deformation capacity (rope failure strain value) of the damaged rope as the percentage of the damage length decreases relative to rope length is illustrated in Fig. 2e, d and 2f, converging to a minimum value equal to 0.063 in this particular case. The reduction in the rope strength and deformation capacity of the damaged rope relative to the intact rope are approximately equal to the damage inflected to rope cross-section (10%) for this particular damaged rope analysis. Accordingly, the model captures the effect of having a weakened cross-section acting over a localized region defined by the recovery length. For cases where the damage length to rope length ratio is small, the damaged capacity curve of the rope coincides with the intact one up the rope failure due to strain localization in its weakened cross-section. Accordingly, the *SLM* can provide an upper bound for the capacity curve of a damaged rope.

2.2. Asymmetric damage distribution model (ADDM)

Beltran and De Vico (2015) proposed a mechanical model to estimate the static response of a rope asymmetrically damaged on its outermost layer. In order to account for the asymmetric damage distribution, the damaged rope is assumed to behave as a nonlinear beam under uncoupled biaxial bending and axial load with Bernoulli's kinematic hypothesis. Biaxial bending arises from the unbalanced radial contact forces within a rope cross-section due to the asymmetric damage distribution, resulting in a net transverse force per unit length of rope q_R, which is decomposed into the principal planes (*xy* and *xz*) of the damaged rope cross-section (Fig. 3a). The magnitude of this net transverse force accounts for the initial helical geometry of the unbroken rope components.

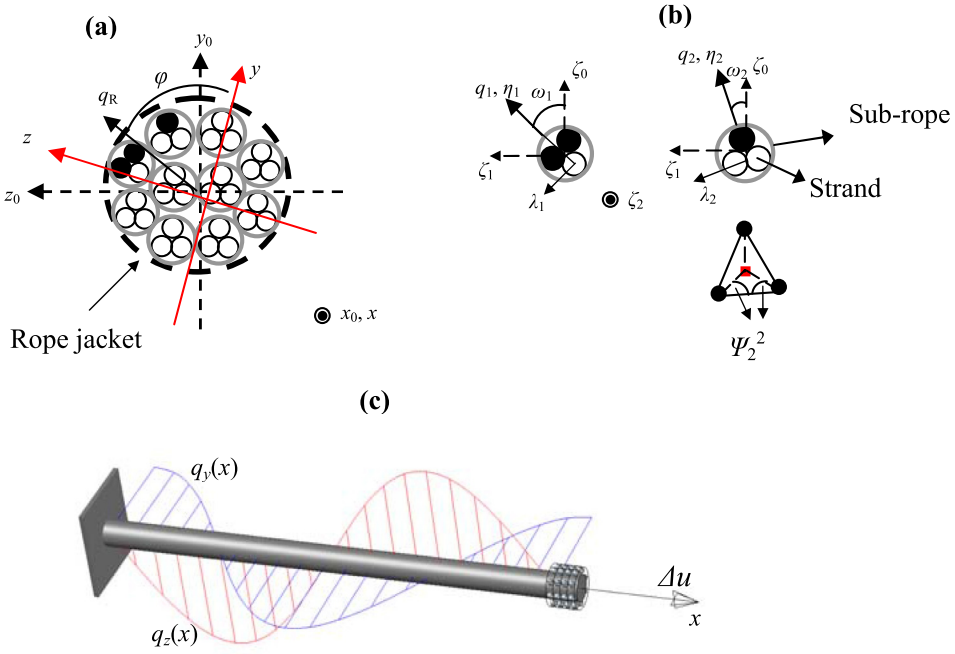

Fig. 3. (a) Asymmetrically damaged rope cross-section; (b) three-strand sub-rope configuration; (c) nonlinear beam under sinusoidal loads.

An iterative cross-sectional numerical algorithm, based upon a displacement control analysis scheme, is implemented to estimate the asymmetric damaged rope capacity curve, stress and strain distributions throughout rope cross-section, and rope geometry deformation for a prescribed axial displacement of the rope. The computation of the force q_R and the numerical examples provided to validate this model are based on simple asymmetrically damaged cross-section geometries: one rope level in which a certain number of rope components are wrapped around a central straight core. In the current study, the proposed model is extended to analyze a more complex rope geometry that consists of a group of parallel sub-ropes in which each sub-rope is built by twisting three strands together as described in the analysis of the *SLM* (Section 2.1).

According to the model proposed by Beltran and De Vico (2015), the static behavior of an asymmetrically damaged rope is governed by the following equations:

$$(EI_{zz})_{\text{sec}}\frac{d^4v}{dx^4} - q_y(x)\left(1+\frac{du(x)}{dx}\right) - H(x)\frac{d^2v}{dx^2} = 0 \tag{3}$$

$$(EI_{yy})_{\text{sec}}\frac{d^4w}{dx^4} - q_z(x)\left(1+\frac{du(x)}{dx}\right) - H(x)\frac{d^2w}{dx^2} = 0 \tag{4}$$

where the plane directions z and y coincide with the principal axes of the damaged cross-section; $q_y(x)$ and $q_z(x)$ are the distributed forces along the rope length in the y and z direction respectively; $(EI_{zz})_{\text{sec}}$ and $(EI_{yy})_{\text{sec}}$ are the secant bending stiffnesses of the rope component with respect to the z and y axes, respectively; $v(x)$ and $w(x)$ are the deflections in the xy and xz (principal) planes, respectively; $u(x)$ is the displacement of the centroid in the axial direction; and $H(x)$ is the horizontal force relative to the axial direction of the undeformed damaged rope.

The procedure implemented to compute the expressions for $q_y(x)$ and $q_z(x)$ is extended relative to the one utilized by Beltran and De Vico (2015) due to the increasing complexity of the damaged cross-section rope analyzed in the current study as previously stated. The process, and related assumptions, of computing the net unbalanced line force q_R for the case of a two-level homogeneous rope (i.e., all rope components have the same material properties) with parallel sub-rope construction, whose damaged cross-section for illustrative purposes is depicted in Fig. 3a, is outlined in the subsequent steps. In the following, the superscripts of the equations refer to the level to which the components belong, and the subscripts refer to the layers where the components are located, except for the local ($\zeta_0\zeta_1\zeta_2$) and global ($x_0y_0z_0$) coordinate system and net unbalanced radial line forces q_1 and q_2.

- Consider the asymmetrically damaged (broken components colored black) rope cross-section depicted in Fig. 3a. Each damaged sub-rope is analyzed as an individual one-level damaged rope to estimate its local radial net unbalanced force relative to the local coordinate system $\zeta_0\zeta_1\zeta_2$ (Fig. 3b). For simplicity, the geometrical parameters of the strands that form each sub-rope (i.e., pitch distance, helix angle, and curvature) are considered to be the same.
- The values of the local net unbalanced radial line forces q_1 and q_2 (Fig. 3b) along the local longitudinal axis of the corresponding sub-rope are given by (Beltran and De Vico, 2015)

$$q_1 = \frac{\kappa_2^2 T_{2,[2]}^2}{\cos\theta_{2,[2]}^2} \tag{5a}$$

$$q_2 = \frac{2\kappa_2^2 T_{2,[2]}^2 \sin\Psi_2^2}{\cos\theta_{2,[2]}^2} \tag{5b}$$

where κ_2^2 is the curvature of a rope component in layer two of the second level of the rope; $T_{2,[2]}^2$ is the axial force of a component in layer two of the second level, which forms a component of the first level, belonging to layer two; $\theta_{2,[2]}^2$ is the helix angle of components that belong to layer two in the second level, which form components of the first level belonging to layer two; and Ψ_2^2 is the angle between the contact line force direction of the rope component in layer two of the second level of the rope, which points to the centroid of the equilateral triangle that forms the three-strand configuration, relative to the base of this equilateral triangle (i.e., 30° in this example, Fig. 3b). In this particular example, the directions of the line forces q_1 and q_2 coincide with the principal axes λ_i, η_i ($i = 1,2$) of the damaged subrope cross-sections (Fig. 3b), and the local reference system $\zeta_{0d}\zeta_1$ is parallel to the global reference system y_0z_0 due

to the type of rope construction (parallel sub-ropes) studied.

- It is assumed that the projections of the line forces q_1 and q_2 point to the centroid of the damaged cross-section; thus, the projection resultant of the net unbalanced line force acting on the cross-section q_R also points to the rope cross-section centroid. In this way, the magnitude of q_R is maximized and any potential torsion induced to the rope cross-section by the unbalanced line forces q_1 and q_2 is ignored (Eqs. (3) and (4) do not include torsional terms). The line force q_R forms an angle φ relative to an arbitrary axis y. Due to the helical nature of the strands, this axis coincides with one of the principal axes of the damaged rope cross-section for increasing values of φ (Fig. 3a) equal to $n\pi/2$ (n is an integer). Considering a damaged cross-section in which the arbitrary xy and xz planes coincide with principal ones (Fig. 3a), the net transverse line forces along the longitudinal axis of the ropes in both the xz and xy (principal) planes are given by

$$q_z = q_R \sin\varphi \tag{6a}$$

$$q_y = q_R \cos\varphi \tag{6b}$$

for a given value of rope axial strain ε_r to compute the displacement field of a generic point of each unbroken rope component (Beltran and De Vico, 2015). The displacement field of a particular generic point at section x can be described using the component displacements $u(x)$, $v(x)$ and $w(x)$ of the damaged rope centroid at same section as follows:

$$u_x(x) = u(x) - y\frac{dv(x)}{dx} + z\frac{dw(x)}{dx} \tag{7a}$$

$$u_y(x) = v(x) \tag{7b}$$

$$u_z(x) = w(x) \tag{7c}$$

where $u_x(x)$, $u_y(x)$, and $u_z(x)$ denote the displacements in the x, y, and z directions, respectively (Fig. 3a), of the generic point ((z,y) location at rope cross-section) under consideration; and $d(\cdot)/dx$ is used for the first derivate. As previously stated, in this formulation the effect of the angle of twist of the rope component on its lateral deflections $v(x)$ and $w(x)$ is neglected. To estimate the static response of a damaged rope, an incremental-iterative numerical procedure is implemented (Beltran and De Vico, 2015) in which the jth increment of the Jth step of the analysis in axial strain of an unbroken strand in layer two of the second level, considering small strain assumption, which forms the subrope t of the first level, belonging to layer k, $[(\delta\varepsilon^2_{2,[k]})_j]_J$, is given by

$$\left[\left(\delta\varepsilon^2_{2,[k]}\right)_j\right]_J(x) = \left[\left(\delta\left(\frac{du(x)}{dx}\right)_t\right) - y_t\left(\delta\left(\frac{d^2v(x)}{dx^2}\right)_t\right) + z_t\left(\delta\left(\frac{d^2w(x)}{dx^2}\right)_t\right)\right]_j\left(\left(\cos\theta^2_{2,[k]}\right)^2\right)_J \tag{8}$$

- The condition that the projection of the resultant net unbalanced line force q_R points to the centroid of the damaged rope cross-section, changing its direction from outward to the interior of the rope cross-section, is met along the rope axis for increasing values of φ (Fig. 3a) equal to $n\pi$ (n is an integer) due to the helical configuration of the strands that form each sub-rope. In order to capture the dependence of the line force q_R on the aforementioned helical nature of strands in the initial rope configuration, the angle φ varies according to the relationship between the local swept angles ω_i ($i = 1,2$) and the helical geometry of the strands (Fig. 3b), i.e., $\omega_i = (2\pi x/p^2_{2,[2]})$, where $p^2_{2,[2]}$ is the pitch distance of rope components that belong to layer two in the second level, which form components of the first level belonging to layer two.

The procedure described accounts for the fact that the sub-ropes are assembled parallel to each other in two layers and they are held together by a jacket; (Fig. 3a). As such, the local longitudinal axis of each damaged sub-rope ζ_2 is parallel to the longitudinal axis of the rope x (i.e., $\cos\theta^1_1 = \cos\theta^1_2 = 1$). The damaged rope is analyzed with a constant cross-section in which the parameters involved in Eqs. (3) and (4) are relative to the principal axes of the cross-section, and the helical nature of rope components of the second level of the rope in the initial rope configuration is captured by the sinusoidal variation of the net transverse line forces $q_y(x)$ and $q_z(x)$ (Fig. 3c).

Once the values of q_y and q_z in Eqs. (3) and (4) are estimated, these equations are analytically solved (i.e., they have closed-form solutions) where δ is the variational operator and the above expression assumes that the deformed configuration of unbroken strands can be accurately estimated by a first-order circular helix curve based upon the work by Beltran and De Vico (2015). Considering that the numerical implementation of the *ADDM* is based on a displacement control scheme, the incremental axial rope displacement δu_r is specified for each step of the analysis. Similarly to the numerical algorithm implemented for the *SLM* case, the size of δu_r for each step of the analysis is also controlled by constraining the computed increment in axial strain for each unbroken rope component $[(\delta\varepsilon^2_{2,[k]})_j]_J$. In this particular study, the criteria arbitrary set is that each value of $[(\delta\varepsilon^2_{2,[k]})_j]_J$, should be less than 2% of the failure strain given by the constitutive law. For the sake of explanation, if this criteria is not met for any iteration of the Jth step of the analysis, sub-steps are performed by continuously bisecting the increment in axial rope displacement $[\delta u_r]_J$ until the criteria are satisfied. The total number of steps, i.e, J_n, carried out in the algorithm is controlled by the maximum failure strain criteria. This criteria is used to establish the onset of failure of any rope component and consequently, at that strain level, estimate the residual strength and deformation capacity of a damaged rope. Typically, the centroid of the tth subrope is considered as the generic point to evaluate the above expression. Assuming unbroken strands behave as fiber elements (i.e., they only develop uniaxial state of stress), and considering a discrete formulation model and linearized incremental constitutive law, the increment in damaged rope axial load for the jth substep of the Jth step of the analysis at the end of the iteration process (*iter*), $[(\delta H)^{iter}_j]_J$, can be estimated as:

$$\begin{aligned}[(\delta H)^{iter}_j]_J = &\sum_t\sum_l((E_l)^2_{2,[k]})_{j-1}\left(\delta\left(\frac{du(x)}{dx}\right)_t\right)^{iter}_j(A_l)^2_{2,[k]}\left(\left(\cos\theta^2_{2,[k]}\right)^3\right)^{iter}_J + \sum_t\sum_l((E_l)^2_{2,[k]})_{j-1}\left(-y_t\left(\delta\left(\frac{d^2v(x)}{dx^2}\right)_t\right)\right.\\ &\left.+z_t\left(\delta\left(\frac{d^2w(x)}{dx^2}\right)_t\right)\right)^{iter}_j(A_l)^2_{2,[k]}\left(\left(\cos\theta^2_{2,[k]}\right)^3\right)^{iter}_J\end{aligned} \tag{9}$$

where the subscripts t and l refer to sub-ropes (first level of the rope) and strand (second level of the rope), respectively; and E_l and A_l are the tangent modulus and cross-sectional area of the particular strand l, respectively. The first term of the above expression accounts for the contribution of all unbroken strands to the increment of damaged rope axial load as the rope were subjected to purely tensile load (expression related to the so-called net-area effect), and the second term is related to the lack of symmetry of the cross-section (asymmetric damaged distribution) that perturbs the straight initial and deformed configuration of the rope (hereafter referred to as the perturbation term) inducing a lateral deformation to the asymmetrically damaged rope and a gradient in the stress/strain distribution throughout a rope cross-section. As a result, premature failure is initiated in the rope due to this gradient in the stress/strain distribution relative to the net-area effect as discussed by MacDougall and Bartlett (2006) and Beltran and De Vico (2015). Consequently, Eq. (9) can be recast in the following form:

$$[(\delta H)_j^{iter}]_J = [(\delta H)_j^{iter}]_{J,netarea} + [(\delta H)_j^{iter}]_{J,pertterm} \tag{10}$$

where the first term of the above expression is related to the net-area effect (*netarea*) contribution and the second term is related to the perturbation term (*pertterm*), associated with biaxial bending acting on the rope that arises due to the lack of symmetry of the cross-section according to Beltran and De Vico (2015). The total axial force developed by the rope the for Jth step of the analysis, $(H)^{iter}_J$, is given by

$$(H)_J^{iter} = \sum_{j=1}^{jmax} [(\delta H)_j^{iter}]_J = \sum_{j=1}^{jmax} [(\delta H)_j^{iter}]_{J,netarea} + \sum_{j=1}^{jmax} [(\delta H)_j^{iter}]_{J,pertterm} = (H)^{iter}_{J,netarea} + (H)^{iter}_{J,pertterm} \tag{11}$$

where *jmax* is the maximum number of increments considered for each step of the analysis (subscript J) due to material and geometric non-linearities, which can vary from one analysis step to another depending on the of the desired accuracy of the results. Based on the formulation proposed, that considers small strain assumption for each step of the analysis performed, the total perturbation term, $(H)^{iter}_{J,pertterm}$, should not contribute to the value of the axial load, $(H)^{iter}_J$, because this term is related to the biaxial bending induced in the damaged rope which assumed to be uncoupled from axial response. The numerical implementation of this formulation, however, considers only one integration point for each unbroken rope component (its centroid) to compute its axial stress to subsequently compute its contribution to the value of the axial load, $(H)^{iter}_J$, through Eq. (9) (Beltran and De Vico, 2015). In order to study the accuracy of the implemented algorithm, the total perturbation term, $(H)^{iter}_{J,pertterm}$, can be expressed in terms of the axial load, $(H)^{iter}_J$, and the total increment in axial load associated to net area effect, $(H)^{iter}_{J,netarea}$, for every Jth step of the analysis to evaluate its impact on the value of the

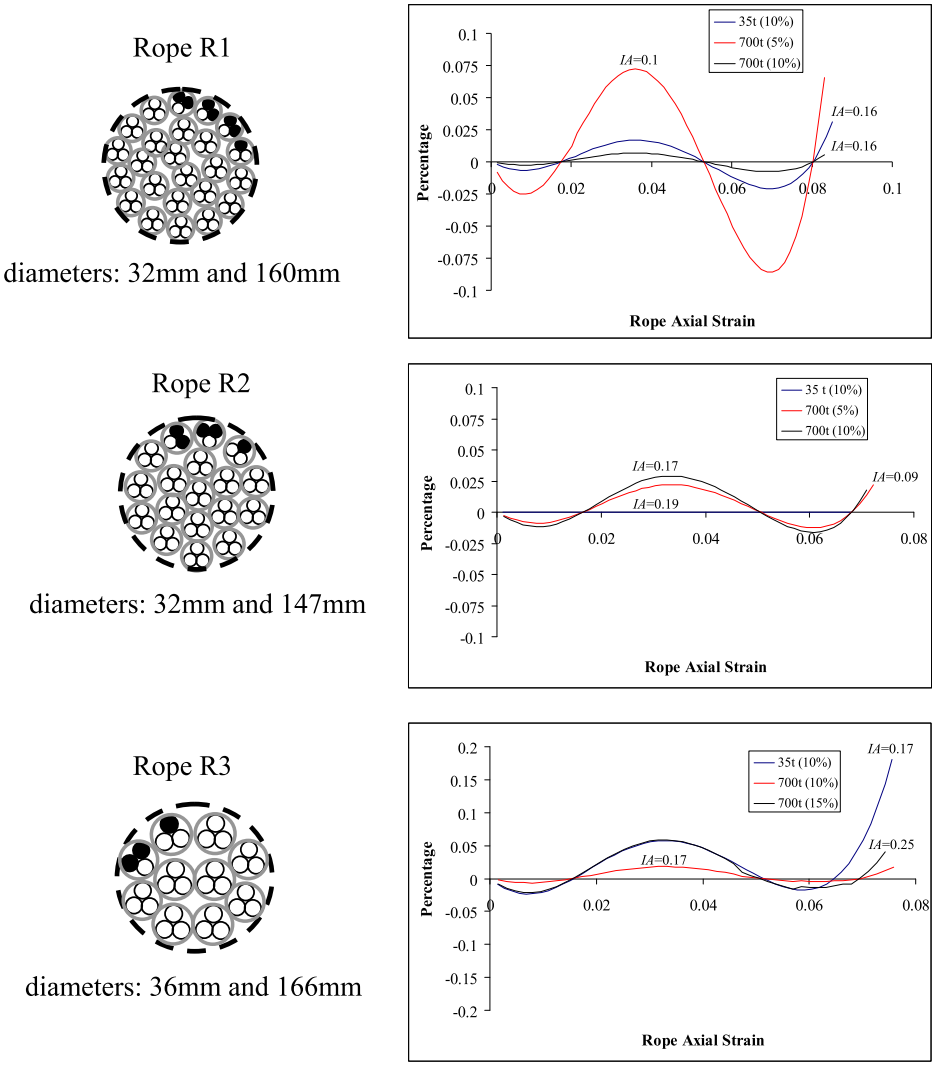

Fig. 4. Impact of perturbation term on damaged rope axial load.

axial load ($(H)^{iter}_j$).

The impact of the perturbation term on the damaged rope axial load (expressed as percentage of this value) for a wide range of axial rope strain values for different type of polyester rope cross-section constructions and damage distributions is presented in Fig. 4. All the rope cross-sections depicted in Fig. 4 have SBS values equal to 35 tonnes and 700 tonnes (6864.6 kN), with diameters that vary from 32 mm to 166 mm as specified in the same figure in which the small and large values correspond to rope cross-sections with SBS values equal to 35 tonnes and 700 tonnes, respectively. Similarly to the proof given for the *SLM*, boundary conditions of the ropes analyzed assume one end section is fully clamped and the other end has a uniformly increasing axial displacement history with no axial twist (Fig. 3c). In order to be consistent with previous works (Beltran and Vargas, 2012; Beltran and De Vico, 2015), the degree of asymmetry of the damaged cross-section is captured by a scalar quantity termed the index of asymmetry (*IA*). This parameter accounts for the shift of the center of stiffness of the damaged cross-section relative to the intact rope cross-section due to the asymmetric distribution of damage. For computational purposes, the initial value of this parameter $(IA)_0$ (computed for small rope axial strain value) is considered as a representative measure of the degree of asymmetry of the rope cross-section (hereafter referred to as *IA*) as extensively discussed by Beltran and Vargas (2012).

The damage level of the damaged cross-sections shown in Fig. 4 varies from 5% to 15%, in which ropes R1 and R3 have the same number of parallel sub-ropes for both SBS values (drawn in the figure). Conversely, cross-section of rope R2 has eighteen parallel sub-ropes for rope with SBS equal to 35 tonnes and twenty parallel sub-ropes for rope with SBS equal to 700 tonnes. The contribution of the perturbation term (Eq. (11)) to the total value of the rope axial load (shown as percentage in Fig. 4) fluctuates around the zero value (horizontal axis) for the entire range of rope axial strain values considered for all the ropes analyzed. The peak values of this fluctuating behavior are quite small in which the maximum magnitude is equal to 0.18% for rope R3 with SBS equal to 35 tonnes and a 10% damage level. Each plotted curve in Fig. 4 has its associated *IA* value according to the damage distribution within a corresponding rope cross-section. Based on the results presented in Fig. 4, for the ropes analyzed in this study in which the diameters vary from 32 mm to 166 mm, damage levels (asymmetrically distributed) range from 5 to 15%, and the corresponding *IA* values vary from 0.09 to 0.25, the contribution of the perturbation term (Eq. (11)) to the total value of the rope axial load is negligible. Consequently, the integration scheme implemented is sufficiently accurate, and the axial load and axial stiffness of these damaged ropes can be readily estimated by the net-area effect model for a given rope axial strain value. As such, the estimated damaged capacity curve (and accordingly damaged rope stiffness) of the rope given by the *ADDM* is governed by the net-area effect term providing a more flexible response relative to the intact one and consequently a lower bound for the damaged capacity curve when compared with the predicted curved given by the *SLM*. The values of the residual strength and deformation capacity of these ropes, however, differ from the ones predicted by the net-area effect model as discussed in the subsequent section.

3. Numerical simulations and discussion

Based upon the results presented in Section 2, both numerical models, *SLM* and *ADDM*, provide an upper and lower bound, respectively, for the predicted capacity curves of the analyzed asymmetrically damaged polyester ropes. In this section, these two models are used to estimate the stiffness, residual strength, and axial failure strain of a set of large-scale damaged polyester ropes tested by Ward et al. (2006). As previously stated, these two latter values are based on the maximum strain failure criteria considering the axial failure strain values of the strands, which are the smallest defined structure in rope constructions. Additionally, estimated and measured values are compared to validate the proposed

Table 1
Predicted and measured residual strength and failure strain values of damaged ropes.

Rope	SBS (kN)	% Damage	Axial Failure Strand Strain	SLM		ADDM		Exp 1		Exp 2		Exp 3		Intact Rope Predicted		Intact Rope Measured	
				Residual Strength (kN)	Failure Strain	Residual Strength (kN)	Failure Strain	Residual Strength (kN)	Failure Strain	Residual Strength (kN)	Failure Strain	Residual Strength (kN)	Failure Strain	Residual Strength (kN)	Failure Strain	Residual Strength (kN)	Failure Strain
R1	343.2	10	0.084	288	0.078	274	0.085	311	0.087	314	0.08	285	0.082	321	0.087	320	0.09
R2	343.2	10	0.067	308	0.063	314	0.068	–	–	–	–	–	–	345	0.069	347	0.071
		12	–	–	–	299	0.068	307[a]	0.069[a]	–	–	–	–	–	–	–	–
		17	–	–	–	286	0.068	–	–	263[b]	0.062[b]	–	–	–	–	–	–
R3	343.2	10	0.081	341	0.076	309	0.076	–	–	372	0.078	365	0.076	380	0.083	383	0.086
		13.3	–	327	0.078	–	–	324[c]	0.079[c]	–	–	–	–	–	–	–	–
R1	6864.6	25	0.084	5658[e]	0.075[e]	5660	0.087	5306[d]	0.07[d]	–	–	–	–	7551	0.087	–	–
		25	–	5649[f]	0.066[f]	–	–	–	–	–	–	–	–	–	–	–	–
R2	6864.6	10	0.074	6077	0.069	5534	0.071	–	–	–	–	–	–	6764	0.076	6674	0.077
		20	–	5378[h]	0.064[h]	–	–	5384[g]	0.064[g]	–	–	–	–	–	–	–	–
R3	6864.6	15	0.077	5755	0.069	5408	0.074	6051	0.075	–	–	–	–	6790	0.079	6834	0.082

SBS: specified breaking strength.
SLM: strain localization model.
ADDM: asymmetric damage distribution model.
[a] Intermediate failure reported during experiment. Damage to rope increases from 10% to 12%.
[b] Failure during storm loading, prior capacity test. Damage to rope increases from 10% to 17%.
[c] Intermediate failure reported during experiment. Damage to rope increases from 10% to 13.3%.
[d] Failure during storm loading, prior capacity test. Damage to rope increases from 10% to 25%.
[e] Partial effect of strain localization assumed by the *SLM*: SLM- 1 curve (Fig. 6a).
[f] Full effect of strain localization assumed by the *SLM*: SLM- 2 curve (Fig. 6a).
[g] Intermediate failure reported during experiment. Damage to rope increases from 10% to 20%.
[h] Partial effect of strain localization assumed by the *SLM*: SLM- 2 curve (Fig. 6b).

numerical models and explain the tested ropes' behavior. A summary of the failure axial strain values of the strands that form the ropes and the residual strength and failure strain values given by both models, along with available experimental data, are given in Table 1. A discussion of the results presented in this table is given in the subsequent paragraphs.

The test procedures (Ward et al., 2006) involved the following sequential steps: (a) initial cycling to bed-in the ropes; (b) inflict prescribed damage level to ropes; (c) damaged ropes are cycled to simulate storm loading; (d) examination of ropes for any damage progression after storm loading simulation; and (e) perform rope capacity tests. For each type of rope construction, test procedure steps from (c) to (e) were carried out for both undamaged and damaged ropes. Undamaged rope test data (step (e) of test procedures) are used to predict the residual strength of damaged ropes and to estimate the constitutive law of strands (smallest structure defined in rope constructions) after storm loading simulation using the following expression (McKenna et al., 2004):

$$E_{t(rope)} = E_{t(strand)}\left(\cos^{4.75}\theta_1 \cdot \cos^{4.75}\theta_2\right) \tag{12}$$

where $E_{t(\text{rope})}$ and $E_{t(\text{strand})}$ are the tangent modulus of the rope (slope of the measured undamaged rope capacity curves) and the strands that form the ropes respectively; and θ_i is the helix angle of rope level i ($i = 1$ for sub-ropes and $i = 2$ for strands) according to the rope construction model used in this study. The values of θ_i for each rope construction analyzed are estimated from the information provided by Ward et al. (2006) regarding the construction of the sub-ropes that form the ropes. For the case of ropes R1 and R2, the value of θ_2 is estimated as 12°, and it is estimated to be 10° for both SBS values. The value of the helix angle θ_1 is 0° for all ropes due to their parallel sub-rope construction type. For computational purposes, the normal stress of a strand is expressed as a function of its normal strain by using a polynomial function up to the fifth degree (Beltran and De Vico, 2015). As previously stated, for simulation purposes both models consider one end section of the rope to be fully clamped and the other end section to be subjected to a uniformly increasing axial displacement with cross-sectional rotation prevented.

In Fig. 5, predicted and measured capacity curves for three types of rope construction (R1, R2, and R3 previously described in Fig. 4) are presented. These ropes had an SBS equal to 35 tonnes and an initial damage level of 10% of the cross-section, where the damaged was inflicted asymmetrically. The values of the *IA* associated with the initial inflicted damage vary from 0.16 to 0.19 as presented in Fig. 4. These tests considered L/d ratios ranging from 40 to 1000, where L is the rope length and d is the rope diameter. The curves given by the *SLM* are the stiffest response the proposed computational model provides based on the discussion presented in Section 2.1. *SLM* curves account for a strain localization zone around the failure section (rope midspan) induced by rope jacket confinement and/or the effect of rope termination, because both effects limit the damage length due to confinement action. Accordingly, damaged ropes are discretized into three axial-torsional elements (discretization consistent with the description of the *SLM* in Section 2.1, Fig. 1) in which the central element of each rope discretization is the localized region where strain concentrates along the rope length. In all the rope analyses presented in this figure, measured (Exp. data-when available) and predicted curves of intact (initially undamaged) ropes compare quite well between each other in which the rope strengths are accurately predicted and rope failure strains are underestimated by less than 3% with respect to the measured data. This conclusion validates the use of Eq. (12) to estimate the constitutive law of rope components (strands) of each rope analyzed. Associated with the *ADDM*, the values of the net unbalanced line force q_R are quite similar for all the ropes analyzed, ranging from 0 to 650 kN/m.

For the case of rope type R1 (Fig. 5a), all the experimental curves compare well with the *ADDM* curve for small values of rope axial strain (less than 0.03). For greater strain values, all these curves get stiffer and approach the *SLM* curve. Exp. data 1 ($L/d = 40$) and Exp. data 3 ($L/d = 1000$) curves failed at the induced damage location (rope midspan), while Exp. data 2 curve ($L/d = 290$) failed at one end splice (Ward et al., 2006). In the latter, stress concentration could have developed in the failure region that would explain the extra stiffness shown in this curve relative to the *SLM* curve close to the failure strain. The *SLM* curve is an upper bound for the Exp. data 1 and Exp. data 3 curves, meaning the stiffening process experienced by these experimental curves is less steep than the predicted one, thereby allowing an increased deformation capacity (value approaching to the one specified for the intact case). In terms of the residual strength and failure axial strain, experimental values are estimated, respectively, in the range of −8% to +1% and −10% to −2% by the *SLM*.

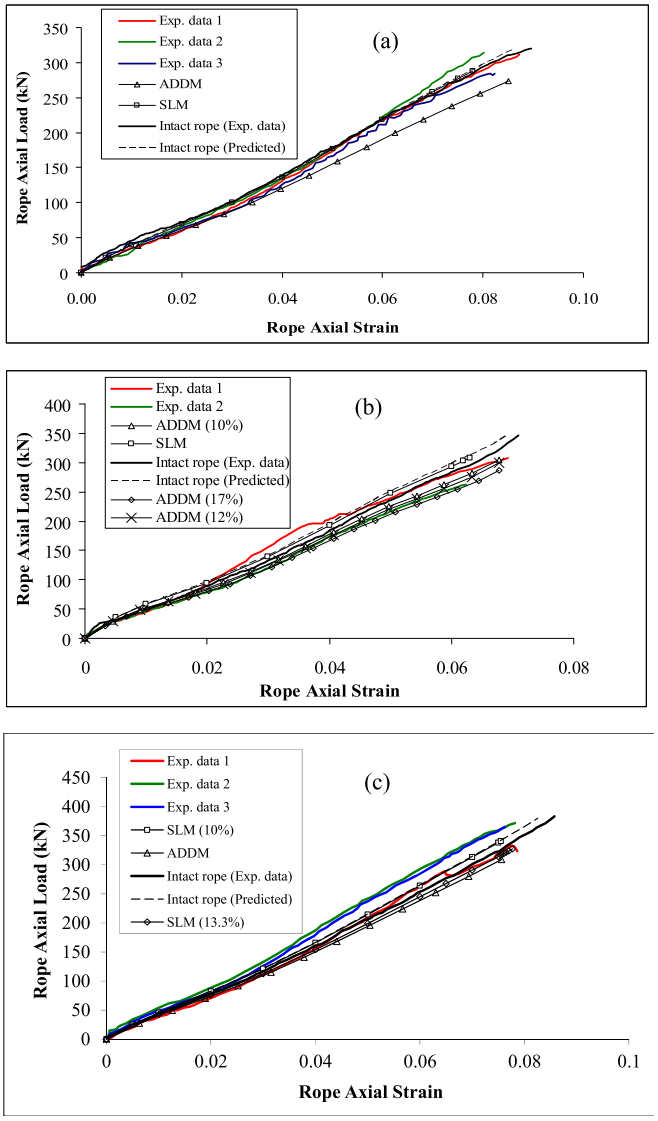

Fig. 5. Capacity curves of initially damaged ropes with SBS equal to 35 tonnes: (a) type Rope R1; (b) type Rope R2 and (c) type Rope R3

Regarding the case of rope type R2 (Fig. 5b), both tested ropes failed near the initially damaged region according to Ward et al. (2006). Exp. data 1 ($L/d = 290$) curve experiences a stiffening process from axial deformation equal to 0.02 to 0.05. In this strain range, it compares well with the *SLM* curve, although it is stiffer over portions of this strain interval. For axial strain values greater than 0.05, this experimental curve softens (failure initiation reported at a load of approximately 196 kN) converging to the *ADDM* (12%) curve. This last curve assumes that the intermediate failure reported corresponds to one extra strand cut based

upon the measured residual strength relative to the measured rope capacity (intact rope). The *IA* value increases from 0.19 to 0.21, and the *ADDM* (12%) underestimates the measured residual strength and failure axial strain by 2.7% and 1.7%, respectively. Exp. data 2 ($L/d = 1000$) curve is softer than the simulations (*SLM* and *ADDM* (10%)) curves. It was reported that some noise was heard during cycling (storm loading simulations). The initial damage (10%) is distributed in three sub-ropes, and these three sub-ropes appeared to have failed during storm loading. Three broken sub-ropes out of 18 correspond to 17% of damage, and the *IA* increases from 0.19 to 0.27. The *ADDM* (17%) curve associated with this damage level compares quite well with the Exp. data 2 curve, although failure strain and residual strength are overestimated by 12% and 10% respectively.

Lastly, for the case of rope type R3, Exp. data 2 ($L/d = 590$) and Exp. data 3 ($L/d = 1000$) curves are stiffer than *SLM* curve for most of the axial strain range. The explanation of this behavior relies on the fact that all the sub-ropes associated with Exp. data 2 curve failed near one splice (stress concentration stiffens rope response), and Exp. data 3 corresponds to a case where an unwinding process took place near the midspan failure location, leading to a stiffer rope response as reported by Ward et al. (2006). Exp. data 1 ($L/d = 40$) curve compares well with the *ADDM* curve up to a strain equal to 0.045, then it experiences a stiffening process and compares quite well with the *SLM* curve up to strain value equal to 0.065. It is reported that some strands failure occurred as this deformation (probably due to stress concentration near one splice), and this curve approaches the *SLM* (13.3%) curve that accounts for one extra strand cut relative to the initial damage. This latter curve underestimates the measured residual strength and failure strain by less than 0.5%. For this tested rope, six sub-ropes failed at the rope midspan and four failed near one of the splices, indicating that the confinement effect associated with a rope jacket or rope terminations (or both) induced strain localization at the cut location.

Based on the analyses presented in Fig. 5, information provided by Ward et al. (2006), and previous studies on strain localization in damaged ropes (Beltran and Williamson, 2011), different stiffening effects (stress concentrations, unwinding, and jacket confinement) impact the manner in which a rope fails. Thus, it is not clear how the response of a damaged rope depends upon the L/d parameter. A more extensive set of experimental data is needed to study the potential dependence of damaged rope response on the L/d parameter, considering different types of rope constructions and variations in damage level to rope cross-section, damage distribution (index of asymmetry), and rope sizes.

Similarly to the analyses presented in Fig. 5, predicted and measured capacity curves of the types of rope constructions R1, R2, and R3, previously described in Fig. 4, are presented in Fig. 6 for ropes with an SBS value equal to 700 tonnes and an initial damage level varying from 10% to 15% of the cross-section, where this damage is asymmetrically distributed. The values of the *IA* associated with the initial inflicted damage vary from 0.16 to 0.25 as presented in Fig. 4, and rope discretizations, based on the *SLM*, are the same as the ones used for the damaged ropes with SBS equal to 35 tonnes (Fig. 5). The tests of these types of ropes consider a fixed value of the parameter L/d, which was equal to 40. Regarding the simulations performed with the *ADDM*, the value of the net unbalanced line force q_R ranges from 0 to 2300 kN/m for rope R2, and it ranges from 0 to 3900 kN/m for rope R3. For the case of rope R1, the value of q_R vanishes due to the particular distribution of damage and rope construction (parallel sub-rope configuration) as discussed subsequently. For the case of rope type R1 (Fig. 6a), Ward et al. (2006) reported that after cycling the rope (step (c) of the test procedures), inspection revealed six sub-ropes were broken. The initial inflected damage to the rope cross-section was 10% and was distributed to four sub-ropes. Hence, it is assumed that the initial partially damaged sub-ropes are within the six broken sub-ropes after cycling, which means that 18 strands are broken, corresponding to 25% of the area damaged prior performing the

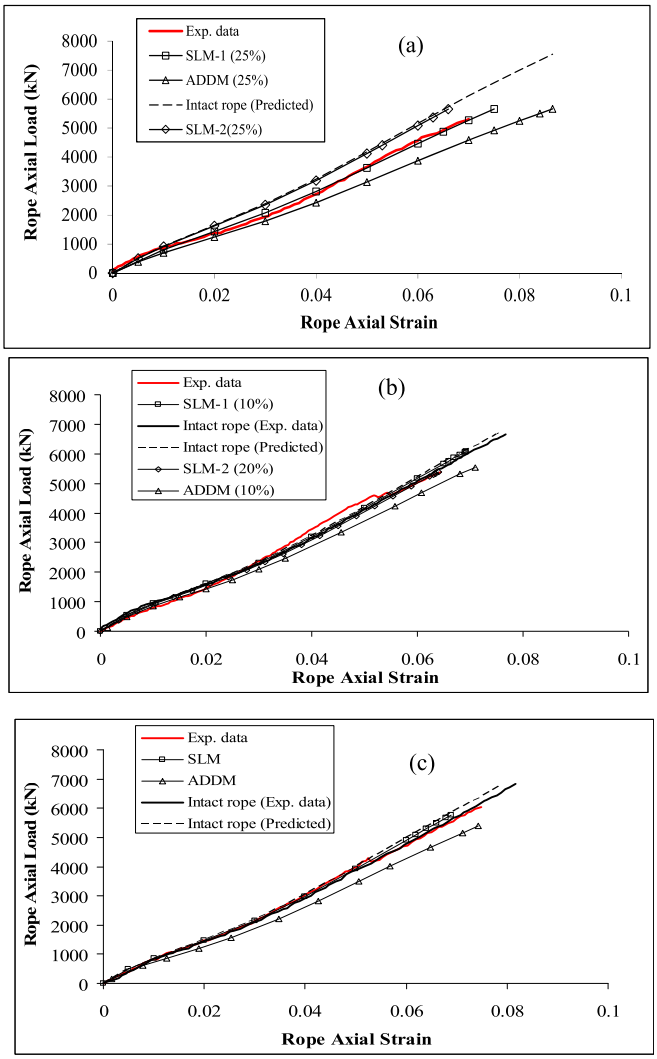

Fig. 6. Capacity curves of initially damaged ropes with SBS equal to 700 tonnes: (a) type Rope R1; (b) type Rope R2 and (c) type Rope R3

capacity test. In this way, asymmetry in damage distribution does not induce transverse load q_R because all the strands that form the damaged sub-ropes are cut. Thus, for this particular case, the *ADDM* coincides with the net-area effect model. The predicted response curves *SLM*-2 and *ADDM* (with an *IA* value equal to 0.3) bound the response of the Exp. data curve in which the former curve is the stiffest response that the strain localization model provides (approaches the intact rope response). The Exp. data curve appears to develop some degree of stiffening relative to the *ADDM* curve, a phenomenon that is well captured by *SLM*-1 curve. This latter curve considers a partial effect of strain localization, simulated by increasing the percentage of the damage length (Section 2.1) of the rope relative to the rope length, on rope response and overestimates by 6% and 7% the residual strength and failure strain, respectively. The tested rope failed due to the splice condition as reported by Ward et al. (2006), which could have induced, due to stress concentrations, the premature failure of the rope relative to predicted values.

For the case of rope type R2 with SBS equal to 700 tonnes (Fig. 6b), the predicted intact curve matches well with the experimental intact rope curve in which the rope strength and failure strain are overestimated and underestimated by 1%, respectively. This rope was initially damaged by 10% of its cross-section, which corresponds to six strands cut and distributed to three sub-ropes. The experimental

damage curve (Exp. data) compares well with *ADDM* (10%) up to a strain equal to 0.025, then it experiences a stiffening process resulting in a response that is a little stiffer than the SLM-1 (10%). There are two failures that soften the rope response, which is bounded by the *SLM*-1 (10%) and *ADDM* (10%) curves before its complete rupture. Based on the measured residual strength of the rope, it can be concluded that the two failures observed in the plot correspond to two broken sub-ropes, which adds six broken stands to the first six. Therefore, 12 broken strands correspond to a 20% damage level, a value that coincides with the measured residual strength. The *SLM*-2 (20%) curve, considering 20% of damage distributed to five sub-ropes and a partial effect of strain localization (phenomenon explained in the discussion of Fig. 6a) compares quite well with last part (after breakage) of the Exp. data curve. Both the measured residual strength and failure strain are underestimated by less than 0.1%. The tested rope failed at the inflicted damaged region as reported by Ward et al. (2006).

In Fig. 6c, the analysis rope type R3 with a 15% initial damage level and an SBS value equal to 700 tonnes is presented. The predicted intact curve matches well with the experimental intact rope curve in which the measured residual strength and failure strain are underestimated by 1% and 2%, respectively. The initial damage inflicted corresponds to 4.5 strands cut and distributed to three sub-ropes. Exp. data curve develops a stiffening process, comparing quite well with the *SLM* curve up to strain equal to 0.053. At this strain level, Ward et al. (2006) report that one sub-rope failed. Assuming this broken sub-rope was partially damaged (two strands cut out of three) in conjunction with the initial damage the rope, its failure adds one more strand cut to the total damage of the rope cross-section, reaching a value of 18% of the total cross-section. The measured residual strength is approximately 88% of the measured intact rope strength, and the measured failure strain value is equal to 0.075. These two values suggest that after the failure of the sub-rope, the rope developed an unwinding process and was able to reach a greater residual strength and failure strain relative to the ones provided by the *SLM* curve.

4. Conclusions

In this paper, two effects that govern static damaged rope response were studied using two different numerical models: strain localization around the failure region and asymmetric damage distribution at a given rope cross-section. The analyses conducted to capture these two effects were uncoupled in order to quantify independently the relevance of each effect on damaged rope stiffness, rope residual strength, and rope deformation capacity. The formulation of each model was described and computationally implemented. Computed results were compared to available test data for a set of large-scale, polyester damaged ropes to validate the models and to explain the tests results obtained.

Most of the initially damaged ropes with an SBS value equal to 35 tonnes, and all the initially damaged ropes with an SBS value equal to 700 tonnes, experienced a stiffening process relative to the *ADDM* (lower bound) curve. This stiffening process, which is primarily induced by the confinement of the rope jacket and end splice effects (especially on shorter ropes ($L/d = 40$)), is well captured by the *SLM* curves because both effects eventually result in admissible recovery length values of the broken strands. The ability of broken rope components to eventually resume carrying load is an important feature of the *SLM* (strain localization model). For these cases, the predicted reduction in rope capacity is similar in magnitude to the loss of cross-sectional area induced through initial damage. The predicted reduction in rope deformation capacity ranges from 7% to 16%, relative to the intact rope response, for cases with initial cross-sectional damage ranging from 10% to 25% of the total cross-sectional area. The unwinding process of the broken strands, however, is not accounted for the *SLM* curves; thus, damaged rope response is underestimated by the *SLM* curves when unwinding of the unbroken strands is the primary stiffening effect.

The response of two rope samples of type R2, with an SBS value equal to 35 tonnes, was accurately predicted by the *ADDM* curves. One of these samples, $L/d = 290$, initially presented a stiffening process, then an intermediate failure occurred during testing. Consequently, the damaged rope response softened and converged to the *ADDM* (12%) curve with an *IA* value equal to 0.21. This index of asymmetry (*IA*) accounted for a greater damage level than the initial value inflicted (10%) due to the previously described intermediate failure that occurred during testing. For this case, the model predicts a reduction of 15% for the rope strength and 3% for the deformation capacity relative to the intact values. The *ADDM* (12%) underestimates the measured residual strength and failure axial strain by 2.7% and 1.7%, respectively. The other rope sample, $L/d = 1000$, experienced the failure of some strands during storm loading simulation. The *ADDM* (17%) curve that considered 17% of the cross-section damaged and an *IA* value equal to 0.27 reasonably predicts the damaged response up to failure, although the measured failure strain and residual strength are overestimated by 12% and 10%, respectively. In this case, the model predicts reductions of 18% of the rope strength and 3% of the deformation capacity relative to the intact values predicted.

It is worth mentioning that both models utilized in this study are highly efficient. Typically, for each rope deformation increment, five or fewer iterations are needed to meet the convergence criteria associated with each numerical model. Additionally, both models are robust over a wide range of parameters, showing good correlation between measured and predicted damaged rope response for ropes of different sizes and construction types, having a variety of damage levels and distributions.

This paper includes analysis results that consider different types of rope configurations with parallel sub-rope construction, effective damage levels from 5% to 25% of the rope cross-section, variety in damage distribution (index of asymmetry varies from 0.09 to 0.27), and different large-scale rope sizes (rope diameters vary from 32 mm to 166 mm). Based on the computed results, it can be concluded that, in general, the *SLM* and *ADDM* curves bound the experimental data (except for the cases discussed in Fig. 5), with the *SLM* providing an upper bound and the *ADDM* curves providing a lower bound. This conclusion extends the range of applicability of both models that in previous works (Beltran and Vargas, 2012; and Beltran and De Vico, 2015) had been validated for small-scale polyester ropes whose diameter was equal to 6 mm, damage levels were in the range of 11%–55%, and index of asymmetry values varied from 0.093 to 0.54.

Despite the good performance of the models described in this paper, additional comparisons with experimental data on damaged ropes are needed to establish the range of applicability of the *SLM* and *ADDM* and to assess the significance of strain localization and damage asymmetry on rope response. Ideally, future research will consider ropes comprised of materials other than polyester and include a variety of damage levels, damage distributions, and ropes sizes. While these two models can be used to provide reasonable bounds on the response of damaged polyester ropes, the interaction between strain localization and asymmetry in damage distribution are treated as uncoupled phenomena in the current research. Hence, a more general model that also accounts for the coupling between strain localization and asymmetry in damage distribution needs to be explored. This coupled model should consider torsion-axial loads, torsion-bending, and bending-axial load interactions to assure convergence, computational efficiency, and robustness of the corresponding implemented algorithm based on the geometry of rope cross-section and rope's length.

Acknowledgement

This work was supported by FONDECYT (Chile) Grant Nº 1150409. The authors gratefully acknowledge this funding.

Appendix

A. Strain localization model (SLM): numerical algorithm

No closed-form expressions exist to compute the stiffness coefficients (Eq. (1)) due to the nonlinear geometry and potential nonlinear constitutive response of rope components. Accordingly, a numerical procedure is needed to compute these terms. Considering a function $\boldsymbol{G}_i = (G_1, G_2)_i$ such that $(T_i, M_i) = \boldsymbol{G}_i(\lambda, \eta)_i$, the stiffness coefficients can be obtained by computing the gradient of this function. Thus, the stiffness coefficients of the matrix $[\boldsymbol{k}_{sr}]_i$ can be evaluated, for any element S_i, as follows:

$$k_{\lambda\lambda} = \frac{\partial G_1}{\partial \lambda} = \left[\frac{T(\lambda + \delta\lambda, \eta) - T(\lambda - \delta\lambda, \eta)}{2\delta\lambda}\right] \tag{A.1}$$

$$k_{\eta\lambda} = \frac{\partial G_2}{\partial \lambda} = \left[\frac{M(\lambda + \delta\lambda, \eta) - M(\lambda - \delta\lambda, \eta)}{2\delta\lambda}\right] \tag{A.2}$$

$$k_{\lambda\eta} = \frac{\partial G_1}{\partial \eta} = \left[\frac{T(\lambda, \eta + \delta\eta) - T(\lambda, \eta - \delta\eta)}{2\delta\eta}\right] \tag{A.3}$$

$$k_{\eta\eta} = \frac{\partial G_2}{\partial \eta} = \left[\frac{M(\lambda, \eta + \delta\eta) - M(\lambda, \eta - \delta\eta)}{2\delta\eta}\right] \tag{A.4}$$

where the centered differentiation formula is used to evaluate the stiffness coefficients, T and M are the axial force and torsional moment, respectively, and $(\delta\lambda, \delta\eta)_i$ are small perturbations to a prescribed level of deformation $(\lambda, \eta)_i$ for each axial-torsional element S_i. The values of the perturbations $\delta\lambda$ and $\delta\eta$ are found using an iterative process where variations are considered until two consecutive values of the stiffness coefficients are sufficiently close based upon a prescribed tolerance. In this algorithm, these induced perturbations are applied separately (i.e., small perturbations are assumed for one variable while holding the other perturbation equal to zero), generating two different perturbed deformations. The values of T and M are computed using the formulation described by Beltran and Williamson (2005).

From equilibrium considerations, the 4×4 tangent stiffness matrix $[\boldsymbol{K}_{sr}]_i$ of each axial-torsional element S_i, associated with the degrees of freedom u_1, ϕ_2, u_3 andϕ_4 (referred as to the "complete set") described in Fig. 1, can be obtained. Hence, with the 2×2 element stiffness matrix $[\boldsymbol{k}_{sr}]_i$ computed, $[\boldsymbol{K}_{sr}]_i$ can be calculated as follows:

$$[\boldsymbol{K}_{sr}]_i = \begin{bmatrix} [\boldsymbol{k}_{sr}]_i & -[\boldsymbol{k}_{sr}]_i \\ -[\boldsymbol{k}_{sr}]_i & [\boldsymbol{k}_{sr}]_i \end{bmatrix} \tag{A.5}$$

The increments in axial displacements and axial rotations of the individual axial-torsional element as well as the increments in external loads (axial forces and torsional moments) required to induce a prescribed increment in the deformation level of the rope (displacement control analysis) can be obtained by solving the following linearized equilibrium equation of a damaged rope throughout the use of an incremental-iterative numerical procedure:

$$[\boldsymbol{K}_r]_j^{k-1}\{d\bar{\boldsymbol{u}}\}_j^k = \{d\boldsymbol{Q}\}_j^k + \{\boldsymbol{R}\}_j^{k-1} \tag{A6}$$

where the superscript k represents the iterative step, $[\boldsymbol{K}_r]_j^{k-1}$ represents the tangent stiffness of the rope at the end of the (k-1)th iteration (converged state) obtained by assembling the tangents stiffness matrices of each axial-torsional element computed from Eq (A5), $\{d\boldsymbol{Q}\}_j^k$ is the increment in the external load vector of the kth iteration, and $\{\boldsymbol{R}\}_j^{k-1}$ is the unbalanced load vector (axial forces and torsional moments) that represents the imbalance between the existing internal and external loads at the end of the $(k-1)$th iteration.

For each iteration k of each increment j, once the Eq. (A6) is solved, the axial strain and axial rotation for each axial-torsional element are computed. Using the constitutive equation corresponding to the current level of rope deformation, the internal axial force and internal torsional moment on axial-torsional element are obtained. These internal quantities are compared with the corresponding external quantities obtained from the solution of Eq. (A6) (computation of the so-called unbalanced load vector). If the norm of this vector is less than a prescribed tolerance, the iteration process is stopped and a new increment in axial deformation and axial rotation of the rope is given to perform the (j+1) step of the analysis. Otherwise, new iterations are carried out (solution of Eq. (A6)) until the norm of the unbalanced load vector meet the stopping criterion.

References

Beltran, J.F., Williamson, E.B., 2010. Numerical simulation of damage localization in polyester mooring ropes. J. Eng. Mech. 136, 945–959.

Beltran, J.F., Williamson, E.B., 2011. Numerical procedure for the analysis of polyester damaged ropes. Eng. Struct. 33, 1698–1709.

Beltran, J.F., Vargas, D., 2012. Effect of broken rope components distribution throughout rope cross-section on polyester rope response: numerical approach. Int. J. Mech. Sci. 64, 32–46.

Beltran, J.F., De Vico, E., 2015. Assessment of static rope behavior with asymmetric damage distribution. Eng. Struct. 86, 84–98.

Beltran, J.F., Williamson, E.B., 2005. Degradation of rope properties under increasing monotonic load. Ocean Eng. 32, 826–844.

Chaplin, C.R., Tantrum, N., 1985. The influence of wire break distribution on strength. In: Organisation Internationale pour l'Etude de l'Endurance des Cables (OIPEEC). Round table conference. June, Glasgow, Scotland).

Chaplin, C.R., 2005. The fatigue and degradation mechanisms of hoisting ropes. In: Hoist and Haul Conference. Perth, Australia.

Cholewa, W., Hansel, J., 1981. The influence of the distribution of wire rope faults on the actual breaking load. In: Organisation Internationale pour l'Etude de l'Endurance des Cables (OIPEEC), Round Table Conference. June, Krakow, Poland).
Cholewa, W., 1989. Wire fracture and weakening of wire rope. In: Wire Rope Discard Criteria: Round Table Conference. Swiss Federal Institute of Technology (ETH). Institute of Lightweight Structures and Ropeways (September, Zurich, Switzerland).
Evans, J.J., Ridge, I.M.L., Chaplin, C.R., 2001. Wire failures in ropes and their influence on local wire strain behavior in tension–tension fatigue. J. Strain Anal. 36, 231–244.
Foster, G.P., 2002. Advantages of fiber rope over wire rope. J. Indus. Text. 32, 67–75.
Hankus, J., 1981. Safety factor for hosting rope weakened by fatigue cracks in wires. In: Organisation Internationale pour l'Etude de l'Endurance des Cables (OIPEEC), Round Table Conference. June, Krakow, Poland).
Lanteigne, J., 1985. Theoretical estimation of the response of helically armoured cables of tension, torsion, and bending. J. Appl. Mech. 52, 423–432.
Li, D., Miyase, A., Williams, J.G., Wang, S.S., 2002. Damage Tolerance of Synthetic-Fiber Mooring Ropes: Small-scale Experiments and Analytical Evaluation of Damaged Subropes and Elements. Technical Report, CEAC-tr-03-0101. University of Houston.
Lian, Y., Liu, H., Huang, W., Li, L., 2015. A creep-rupture model of synthetic fiber ropes for deepwatwer moorings based on thermodynamics. Appl. Ocean. Res. 52, 234–244.
Liu, X., Lian, Y., Li, L., Zhang, Y., 2015. Experimental investigation on dynamic stiffness of damaged synthetic fiber ropes for deepwater moorings. J. Offshore Mech. Arct. 137, 061401–1-8.
MacDougall, C., Bartlett, F., 2005. Mechanical model for unbonded seven-wire tendon with symmetric wire breaks. J. Eng. Mech. 131, 1239–1247.
MacDougall, C., Bartlett, F., 2006. Mechanical model for unbonded seven-wire tendon with single broken wire. J. Eng. Mech. 132, 1345–1353.
McKenna, H.A., Hearle, J.S.W., O'Hear, N., 2004. Handbook of Fibre Rope Technology (Cambridge, England).
Raoof, M., 1991. Wire recovery length in a helical strand under axial fatigue loading. Int. J. Fatigue 13, 127–132.
Ward, E.G., Ayres, R., Banfield, S., O'Hear, N., 2006. Full Scale Experiments on Damaged Polyester Rope. Technical Report, JIP-fp-1. Offshore Technology Research Center.